



Study on Viscous Fluid Flow in Disordered-Deformable Porous Media Using Hydro-mechanically Coupled Pore-Network Modeling

Min-Kyung Jeon¹ · Seunghee Kim² · Amin Hosseini Zadeh² · Tae-Hyuk Kwon¹

Received: 2 December 2019 / Accepted: 5 May 2020 / Published online: 17 May 2020
© Springer Nature B.V. 2020

Abstract

We investigate viscous fluid flows and concurrent fluid-driven deformations in porous media. The hydro-mechanically (H-M) coupled pore-network model (PNM) is developed, which combines the two-dimensional square-lattice PNM and block-spring model. The single-/two-phase flows into saturated deformable porous media are simulated through iterative two-way coupling method in H-M coupled PNM. A comparison between simulations and laboratory observations on flow patterns, solid deformation behaviors, and pressure responses ensures the validity of our H-M coupled PNM in both single-/two-phase flows. Parametric studies using the validated model examine the effects of mechanical coupling, stiffness of solid particles, the viscosity of invading fluids, injection flow rate, and degree of disorder during immiscible viscous fluid injection. The viscous fluid-driven deformation increases the pore throat size and hence reduces the injection pressure. In particular, the viscosity of invading fluid significantly alters the patterns of fluid propagation and solid deformation, along with a transition from the viscous fingering to the stable displacement with increasing viscosity. Moreover, the structural disorder in porous networks magnifies the irregular flow pattern, the pressure fluctuation associated with Haines jumps, and the poromechanical deformation. The particle-level force analysis delineates two distinct regimes: fluid invasion with no deformation and drag-driven deformation, which depends on the balance between the seepage drag force and the skeletal force. The presented results contribute to a better understanding of the H-M coupled fluid flows during the injection of viscous fluids into disordered-deformable porous media.

Keywords Pore-network modeling · Fluid flow in porous media · Poroelastic deformation · Hydro-mechanical coupling · Soft deformable materials

✉ Seunghee Kim
seunghee.kim@unl.edu

✉ Tae-Hyuk Kwon
t.kwon@kaist.ac.kr

Extended author information available on the last page of the article

1 Introduction

Fluid flows in porous media are often associated with the deformation of the hosting pore structure (i.e., hydro-mechanical coupling) in a wide range of science and engineering applications, from biomedical to energy and geological fields. For instance, the therapeutic strategy of convection-enhanced drug delivery causes the deformation of brain tissues, which is a poro-viscoelastic material (Franceschini et al. 2006; Budday et al. 2015). The deformation of brain tissues alters the permeability and porosity of these tissues, such that this hydro-mechanically (H-M) coupled phenomenon needs to be taken into account for prediction of the injection-driven drug delivery (Støverud et al. 2012). As an example of the energy field, predicting the deformation of the membrane electrode assembly, which is caused by a phase-change-induced flow in a deformable network of flow channels, is critical to design a durable polymer-electrolyte fuel cell (Atrazhev et al. 2013). Moreover, many geological and geotechnical operations related to energy resources and storage, such as geothermal energy extraction, geologic carbon dioxide storage, and hydraulic fracturing for oil and gas production, involve the deformation of porous media during the injection/extraction of fluids (Massonnet et al. 1997; Streit and Hillis 2004; Pan et al. 2016; Mahabadi and Jang 2017; Pandey et al. 2017). Nonetheless, fundamental understanding of such H-M coupled processes during fluid transport in deformable porous media at the pore-scale level is still lacking, probably due to the difficulty of conducting an experimental study with a good visualization and data acquisition. The H-M coupled processes become even more sophisticated when the hosting porous media are structurally disordered, and/or when the involved fluids are more than one.

Pore-network models (PNM) have been widely used to simulate various types of fluid flows in porous media at the pore scale (Fatt 1956; Reeves and Celia 1996; Aker et al. 1998; Blunt 2001). The porous media can be either represented by simple geometry, such as a simple lattice network of tubes and an assembly of tubes and spherical pores or reconstructed from the actual pore structure of a material of interest (Fatt 1956; Maier and Laidlaw 1990; Lindquist and Venkatarangan 1999; Silin et al. 2003; Silin et al. 2011). One advantage of using PNM is that it reduces the computational complexity by eliminating the irregularity of pore structures (Vogel et al. 2005). Attempts to couple fluid flows and mechanical deformations (i.e., H-M coupling) in PNM have been made in several studies only recently (Simms and Yanful 2005; Holtzman and Juanes 2010; Holtzman and Juanes 2011; Kharaghani et al. 2011). For instance, Kharaghani et al. (2011) applied a one-way coupling (fluid-to-solid) by combining the PNM with the discrete element method (DEM) to simulate micro-cracks during drying processes. Holtzman and Juanes (2011) presented a two-way hydro-mechanically coupled PNM for inviscid flows and applied for predicting gas flows in hydrate-bearing sediments. However, there is still a little-to-no effort in PNM that incorporates more versatile two-way H-M coupling during viscous fluid flows in deformable porous media.

In this study, we present an advanced two-dimensional (2D) H-M coupled PNM (or H-M PNM) that incorporates the pressure loss of viscous fluids and the structural disorder of porous media. Our two-way coupled model combines a block-spring (BS) model for the deformation of hosting solid particles and a PNM for the flow of invading fluids. We compare the simulation results with experimental observations. Following the comparison, we employ the H-M PNM simulation to investigate the effects of principal parameters, including the viscosity of a fluid, flow rate, and degree of structural disorder, on the mechanical deformation and fluid propagation. Lastly, the observed flow and deformation patterns are

related to the dimensionless ratios, such as capillary number, viscosity ratio, and particle-level forces, including capillary force, seepage force, and skeletal force.

2 Development of Hydro-Mechanically Coupled Pore-Network Simulation Model (H-M PNM)

2.1 Construction of Pore-Network Model (PNM) and Block-Spring (BS) Model

We construct a 2-dimensional (2D) porous medium using the PNM and BS models to emulate the fluid flow and concurrent deformation/displacement of hosting solids, as shown in Fig. 1. The solid matrix part of this porous medium consists of a monolayer of uniform-sized spherical solid particles with a radius of a . Thereby, the depth of our 2D porous medium is set equal to the thickness of the monolayer (or the grain diameter $2 \cdot a$). The solid matrix is represented by the combination of nodes and nonlinear springs in the BS model. Each node represents the central position of a solid particle, and the positions are determined by the contraction of the surrounding springs. Each solid particle is in contact with other surrounding four particles for simplicity (i.e., square-lattice arrangement). That is, four springs are attached to each node, and thus, the coordination number cn of the system is four. The distance between two nodes is initially set to be twice the grain radius (a) prior to commencing fluid injection. Initially, all springs are equally compressed by the set

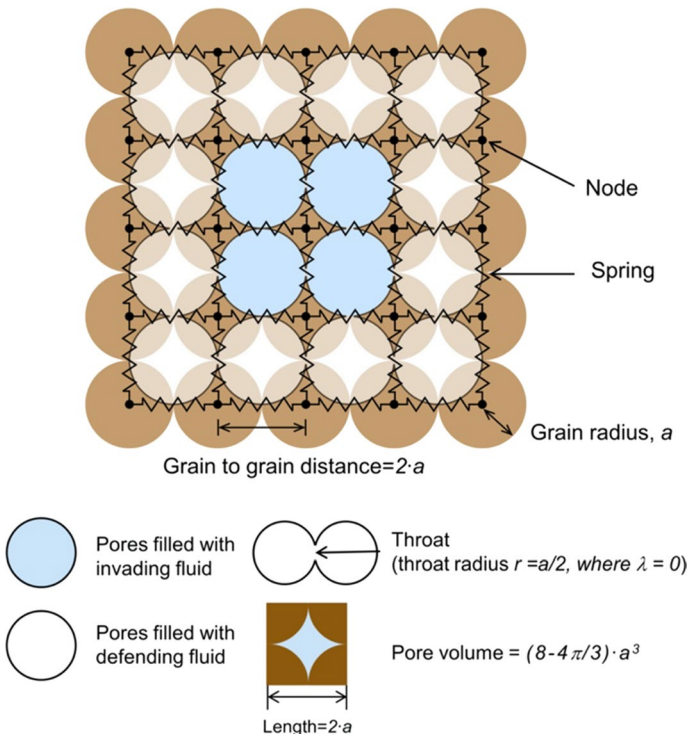


Fig. 1 Schematic illustration of the hydro-mechanically coupled pore-network model

value, h_0 , to simulate isotropic confinement in the solid matrix at the beginning. We set the initial contraction h_0 to be 10% of the radius, i.e., $h_0 = a/10$. The nodes at the outer boundary are fixed at the initial locations during simulation.

The void (pore) part is modeled with a 2D square-lattice pore-network, composed of pores and circular throats (Fig. 1). Each pore represents the pore volume between solid particles. Thus, the pore volume is $(8 - 4\pi/3) \cdot a^3$, equal to the remaining void volume when subtracting a sphere from a cube with an edge of $2 \cdot a$ length. Pores are connected by a throat having the radius r , and this radius determines the permeability k and the capillary pressure p_c of the throat. The permeability is proportional to the square of throat radius by assuming Stokes flow in cylindrical tubes (i.e., $k \sim r^2/8$). The capillary pressure is inversely proportional to the throat radius by Young–Laplace equation (i.e., $p_c \sim 2\sigma/r$, where σ is the interfacial tension). The structural disorder of the system is modeled by using variations in throat radii. The initial and average throat radius value is set to be a half of the particle radius (i.e., $r = a/2$). The radii are randomly generated and assigned to pore throats with the uniform distribution from $(1 - \lambda)a/2$ to $(1 + \lambda)a/2$, where λ is the disorder coefficient $\lambda \in (0, 1)$. The larger disorder coefficient λ means the more heterogeneous system.

2.2 Two-Way Coupling Between Fluid Propagation and Mechanical Deformation

Figure 2 illustrates the two-way H-M coupling algorithm developed in this study. For the fluid-to-solid coupling, the fluid injection causes the rearrangement of solid particles. Such

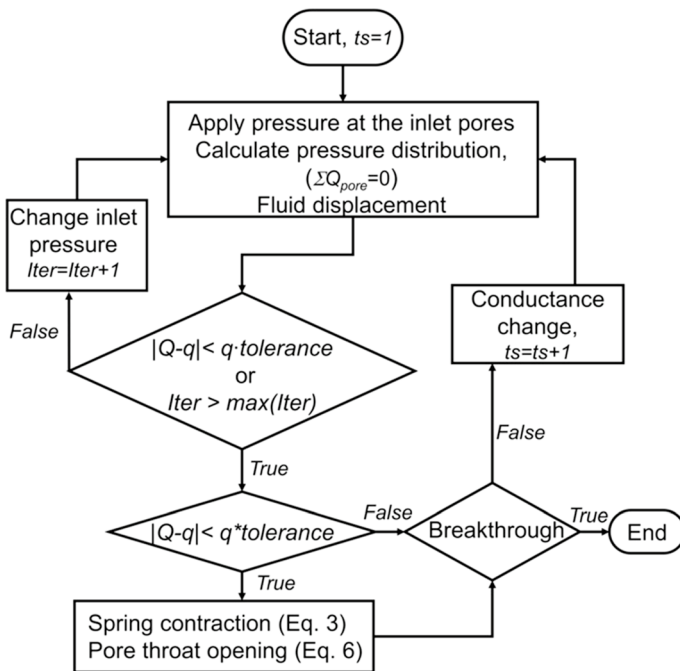


Fig. 2 Algorithm flow of the two-way coupled pore-network simulation under a constant flow rate. *Note:* Q is the calculated flow rate in the simulation, q is the desired flow rate, $Iter$ is the iteration number, ts is the step time number, and *tolerance* is a designated tolerance between Q and q

rearrangement is represented by a change in the spring contraction Δh of the BS model. For the solid-to-fluid coupling, solid medium deformation changes the throat radius Δr of the PNM model, which affects the fluid propagation. We assume that the fluid flow follows Darcy's law:

$$Q = \frac{Ak\Delta P}{\mu_{\text{eff}}l}, \quad (1)$$

where Q is the flow rate, A is the area of the flow channel, ΔP is the pressure difference between pores, μ_{eff} is the effective viscosity of fluids, and l is channel length where the viscous pressure drop occurs ($l = 2a$).

At the beginning of the simulation, a fluid is injected to the four pores located at the center of the pore-network with an injection pressure. Then, the pressure at each pore is calculated based on the mass conservation ($\sum Q_{\text{pore}} = 0$), and the invading fluid propagates toward the outlet. In the case of two-phase flow, the invading fluid advances only when the differential pressure between two pores exceeds the capillary pressure ($\Delta P > P_c$). The fluid propagation simultaneously alters the pore pressure distribution due to the change of the effective viscosity between pores. The effective viscosity is defined as follows:

$$\mu_{\text{eff}} = \alpha\mu_{\text{in}} + (1 - \alpha)\mu_{\text{def}}, \quad (2)$$

where α is the volume fraction of the invading fluid in two pores, μ_{in} is the viscosity of the invading fluid, and μ_{def} is the viscosity of the defending fluid.

The force equilibrium at each node and a specific time t is achieved by the contact forces f_c and the forces exerted by pore pressure f_p . When a pore pressure-induced force in the pore-network changes from $f_p(t)$ to $f_p(t + \Delta t)$, the contact forces at each node also change to achieve a new force equilibrium, and this alters the contractions of the springs connected to the node:

$$\Sigma(f_p(t + \Delta t) - f_p(t)) + \Sigma K\Delta h = 0, \quad (3)$$

where K is the spring stiffness. Herein, the spring stiffness has nonlinear characteristics, determined by Hertzian contact model, as follows:

$$K = 2E^* \sqrt{ah/2}, \quad (4)$$

where E^* is the effective elastic modulus of two solid particles in contact, a is the particle radius, and h is the spring contraction. The effective elastic modulus is defined as follows:

$$E^* = \frac{E}{2(1 - \nu^2)}, \quad (5)$$

where E is the Young's modulus of solid grain and ν is the Poisson's ratio.

Considering the compatibility (i.e., fixed boundary nodes), the position of each node is computed using the spring contraction change Δh from Eq. 3. This particle rearrangement, in turn, results in the change in the throat radius Δr , and this radius change is calculated by assuming the Hertzian contact (Johnson 1987), as follows:

$$\Delta r = -\frac{\Delta h(1 - \epsilon)}{2\sqrt{1 + (1 - \epsilon)^2}}, \quad (6)$$

where ε is the strain of each spring ($\varepsilon = h/l$). This throat radius change alters the fluid propagation by affecting the capillary pressure and the conductance of flow channels.

Constant flow rate conditions are implemented by adjusting the injection pressure through iterations in all simulations. The iteration stops when the difference between the calculated flow rate (Q) and the desired flow rate (q) is less than the tolerance limit, which is set at 15% in this study. Two-phase fluid flows in pore-networks often involve significant pressure differences between pores to overcome the capillary pressure. Therefore, a high flow rate can spontaneously occur, which is also known as Haines jump (Haines 1930). Consequently, this Haines jump inevitably requires large numbers of iterations to achieve a constant flow rate in two-phase fluid flow simulations. Accordingly, we limit the maximum iteration number at 100 to alleviate the computational load, and the injection pressure is chosen from the previous iteration step when the iteration number exceeds the maximum iteration number. The simulation terminates when the invading fluid reaches and fills one of the pores at the outer boundaries, i.e., percolation. The spring is removed when the spring contraction becomes either negative or larger than $2a$ ($h < 0$ or $h > 2a$), which is equivalent to fracture opening.

3 Comparison of the Pore-Network Simulation with Experiments

3.1 Experiment Setup and Materials

We conducted experiments, in which fluid was injected into the deformable porous medium, and the experimental results were compared with the results of the newly developed H-M PNM. Soft hydrogels (SnowReal, JRM chemical, USA) were used to construct the deformable porous medium (MacMinn et al. 2015). Dry hydrogel particles were sieved to prepare the particles with a size from 0.117 to 0.25 mm (passed No. 60 but retained on No. 80 sieve). These dry particles were mixed with water at a weight ratio of 1:200 and then submerged in water for 24 h to allow full swelling of them. The diameter of wet-swollen hydrogels ranged from 0.97 to 1.57 mm with a mean value of 1.18 mm, and the constrained elastic modulus was approximately 50 kPa (Lee and Ryu 2017; Hosseini Zadeh et al. 2019). After that, the fully swollen hydrogels were placed in a circular Hele-Shaw-type cell and the pore spaces were filled with water, as shown in Fig. 3. This Hele-Shaw visualization cell was made of two circular transparent glass plates with a diameter of 280 mm and a thickness of 180 mm separated by a perforated polyurethane rubber (1.59 mm thickness; 86375K132, McMaster-Carr, USA). The perforated rubber confined the hydrogel particles inside and provided a working area of 210 mm diameter with approximately 1.59 mm aperture inside the visualization cell (Fig. 3a). It also allowed the fluid flow, thereby enabling a free drainage boundary condition. Our estimates on the porosity and pore volume inside the cell are approximately 0.4 and 22,030 mm³, respectively. Thereafter, the fluid was injected through a fluid port located at the center of the cell bottom at a constant flow rate of 10 mL/min by using a high-precision syringe pump (PHD Ultra, Harvard Apparatus, USA). The inner diameter of the injection hole was 1 mm (Fig. 3b). The particles' movement and fluid propagation were recorded using a digital camera (Canon EOS Rebel T6i) while monitoring the injection pressure using a pressure transducer (PX302-200GV, Omega, USA) and a data acquisition system (34972A, Keysight, USA).

The invading fluid was either water or mineral oil (BP2629-1, Fisher Scientific, USA) to emulate single- and two-phase fluid flow conditions. The viscosity of mineral oil and water

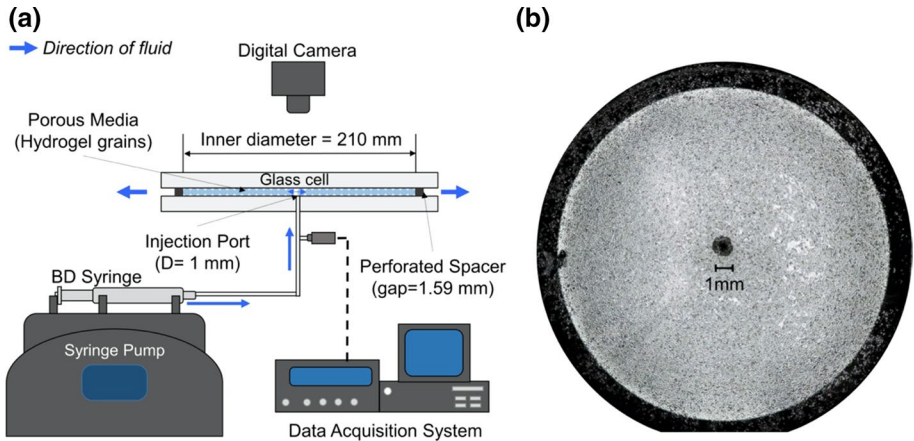


Fig. 3 **a** The experimental configuration and **b** a top view of the visualization cell. Note that the figure is not drawn to scale

under an ambient temperature of $\sim 20\text{--}21$ °C was approximately 28 mPa·s and 1 mPa·s, respectively. Water dyed with soft gel paste (ASG-401, AmeriColor, USA) was injected into the porous medium saturated with undyed water for visualization of fluid propagation in single-phase flow tests. The porous medium was pre-saturated with the dyed water during mineral oil injection in two-phase flow tests. Though the similar refractive indices between water and hydrogel particles hardly allow pore-scale observation, more details on experiment setup and results can be found in Hosseini Zadeh et al. (2019).

3.2 Pore-Network Model and Simulation Condition

We construct a pore-network to retain similarity with the porous medium used in the experiments although there is a fundamental difference of dimension between the experiment and numerical simulation. The size of the pore-network is 80×80 with a total length of 94.4 mm, which is approximately a half of the inner diameter of the test cell. The particle radius a and the effective elastic modulus are assigned as 0.59 mm and 50 kPa, respectively, and these are the approximate values of the soft gels used in the experiment. The depth of network is 1.59 mm to be consistent with the experiment, and accordingly, the total pore volume of the pore-network is 6750 mm^3 . Moderate heterogeneity is taken into account by introducing the disorder coefficient λ of 0.15 in the throat radius with the mean value of 0.39 mm. The applied flow rate is determined as 10 mL/min ($1.67 \times 10^{-7} \text{ m}^3/\text{s}$) to have the same flow rate to the experiments. Single-phase flows are simulated by assuming no capillarity and no diffusion. By contrast, the interfacial tension between mineral oil and water is assumed as 45 mN/m in two-phase flow simulations (Stan et al. 2009).

3.3 Comparison

The single-phase fluid flow condition is first compared, as shown in Fig. 4a–c. Both the results from the PNM simulation and the experiment agree well, in which the injected water propagates radially with no or minimal deformation of solids. In addition, the

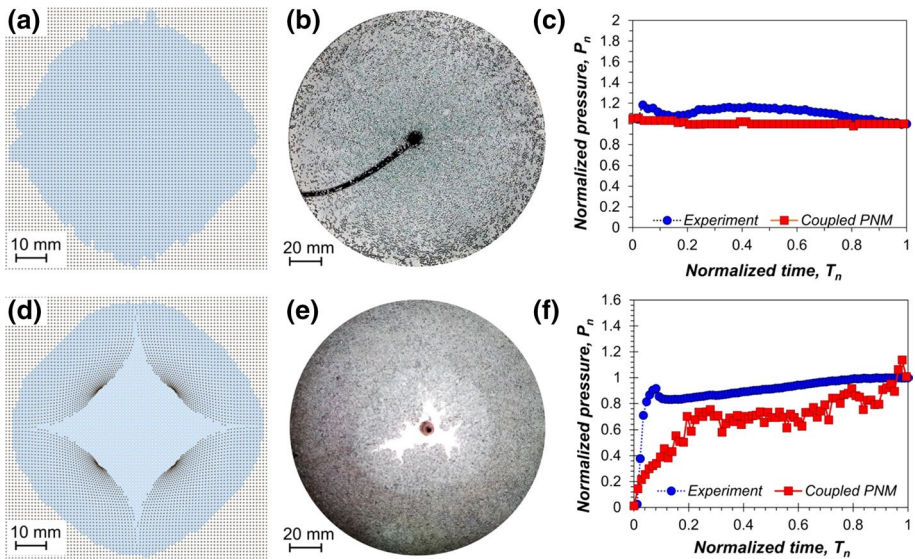


Fig. 4 Comparison between experimental and simulation results. Single-phase fluid injection: **a** the H-M coupled PNM simulation, **b** the experiment using a Hele-Shaw type cell (dyed blue water injection to transparent water), and **c** the normalized pressure (P_n) with respect to the normalized time (T_n) during water injection into a water-saturated medium. Two-phase fluid injection: **d** the H-M coupled PNM simulation, **e** the experiment (mineral oil injection to dyed blue water), and **f** the normalized pressure (P_n) with respect to the normalized time (T_n) during mineral oil injection into a water-saturated medium. Herein, the pressure and time are normalized with the values at percolation, i.e., $P_n = P/P_p$ and $T_n = T/T_p$, where P_p and T_p are the pressure and time at percolation. Note that the captured images (**a**, **b**, **d**, and **e**) were taken when the invading fluid advanced ~ 48 mm away from the inlet port. The invading fluid is colored with blue in the PNM simulations

injection pressures stay almost constant until percolation, and these pressure responses also show a good agreement between the simulation and experiment.

The two-phase flow condition, where oil is injected in a water-saturated porous medium, exhibits different behaviors due to the presence of the capillarity and flow-induced deformation, as shown in Fig. 4d–f. Both simulation and experiment results show that the injected mineral oil propagates radially and at the same time substantial deformation of solid particles takes place near the inlet (Fig. 4d, e). The injection pressures show gradual increases during the fluid injection both in the simulation and experiment, which is due to the viscous drag caused by high viscosity oil (Fig. 4f).

These comparisons support that our H-M PNM can effectively capture the pattern of fluid propagation, concurrent fluid-driven deformation, and pressure responses in both single- and two-phase fluid flows in deformable porous media though there are some limited capabilities. However, careful discretion is required when attempting to examine the shape of poromechanical deformation because the coordination number ($cn=4$) has a predominant effect on the deformation shape.

Meanwhile, it is worth noting that at the beginning of oil injection, a sharp pressure drop is observed in the experiment, associated with mechanical deformation (Fig. 4f). With oil injection at a constant flow rate, deformation within a soft deformable medium suddenly creates fracture-like cavity and opens pore space. With the moderate flow rate used in the experiment, this pore opening causes a sudden drop in fluid pressure. In other

words, this pressure drop can be explained with a flow-inertial effect caused by pore opening. Through the repeated experiments, this kind of an initial pressure drop is consistently observed when flow-induced deformation occurs, though its magnitude differed. Thereafter, the injection pressure gradually increases due to the viscous drag caused by high viscosity of the invading fluid (oil). On the other hand, such a sudden pressure drop is not captured in the simulation, which is one limitation of our model. As our model assume that the deformation does not change the pore volume but only increases the size of throat radius, the initial pressure drop, associated with a deformation-induced flow-inertial effect, is not captured in the simulation.

4 Results and Discussion

We used the 2D H-M PNM simulation to elucidate the effects of mechanical coupling, the stiffness of solid particles, fluid viscosity, injection rate of fluid, and structural disorder on fluid flows in deformable porous media. Emphasis is given on fluid propagation, solid medium deformation, and injection pressure change. Table 1 summarizes the input parameters and their variations.

4.1 Effects of Hydro-mechanical Coupling and Particle Stiffness

Poromechanical deformation of hosting porous media has been hardly considered in most of the previous pore-network simulations. However, the poromechanical deformation may not be trivial in soft deformable porous media. Herein, Fig. 5 compares the H-M coupled PNM simulation result and the uncoupled-flow only PNM simulation result, which elucidates the influence of such H-M coupling.

The fluid flow patterns show insignificant difference between whether or not the mechanical deformation is considered (Fig. 5b, c). On the other hand, as the deformation occurs, the injection pressure decreases compared to the case with no deformation. Noting

Table 1 Input parameters for the hydro-mechanically coupled pore-network simulations

Input parameter	Values	Ranges for parametric study
Size of pore-network	50 × 50	–
Grain radius, a	1 mm	–
Average throat radius, r	0.5 mm	–
Effective elastic modulus, E^*	500 kPa	250 kPa, 500 kPa, 5 MPa, and 50 MPa
Viscosity of invading fluid, μ_{in}	28 mPa·s	0, 0.01, 0.1, 1, and 28 mPa·s
Viscosity of defending fluid, μ_{def}	1 mPa·s	–
Flow rate, q	10^{-6} m ³ /s	10^{-10} , 10^{-8} , and 10^{-6} m ³ /s
Disorder coefficient, λ	0.3	0, 0.1, 0.3, 0.5, 0.7, and 0.9
Interfacial tension, σ	45 mN/m	–
Total pore volume	9528 mm ³	–
Porosity, n	0.476	–

The throat aperture is randomly assigned as a function of the disorder coefficient λ with a uniform distribution from $(1 - \lambda)a/2$ to $(1 + \lambda)a/2$

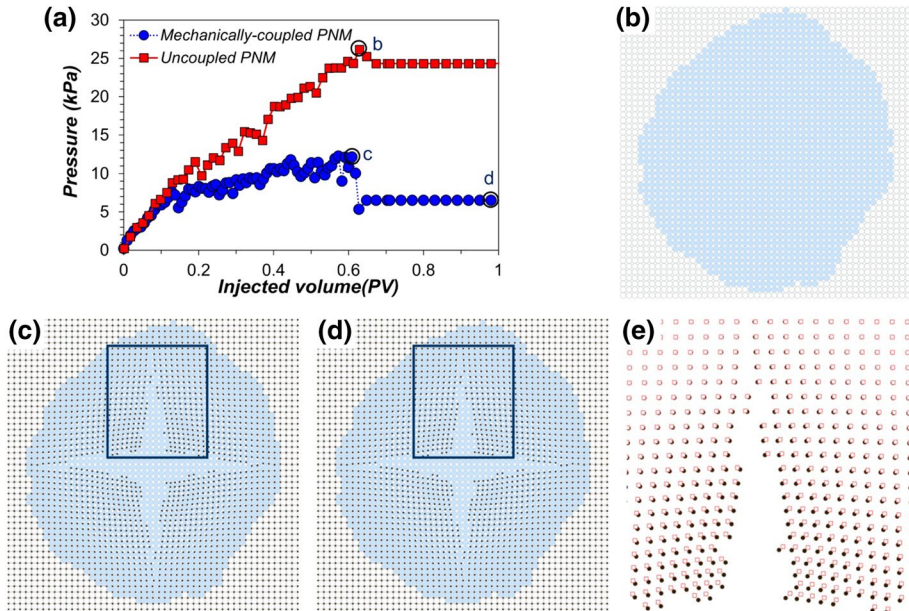


Fig. 5 Effect of hydro-mechanical coupling. Mineral oil is injected at $10^{-6} \text{ m}^3/\text{s}$ into a water-saturated disordered pore-network ($\lambda=0.3$). **a** Evolution of the injection pressures with respect to the pore volume (PV) of injected fluid. Fluid propagation and solid deformation: **b** at percolation in uncoupled PNM, **c** at percolation in H-M coupled PNM, and **d** after percolation in H-M coupled PNM. These snapshots (**b**, **c**, **d**) are taken at the times denoted with black hollow circles in Panel (a). **e** An enlarged image of deformed areas, which depicts the deformation recovery after percolation (red square: at percolation, black dot: after percolation)

that the injection pressure of immiscible fluid is governed by capillary pressure determined by pore throats, this reduced injection pressure in H-M coupled PNM is attributable to the widening of pore throats associated with mechanical deformation. As a result, the widened pore throats lead to the less capillary pressure and the less injection pressure required to maintain the given flow rate when injecting immiscible fluid (Fig. 5a). Therefore, the pressure gradient induced by an immiscible fluid flow causes mechanical deformation of porous media, which again facilitates fluid conduction with a reduced injection pressure. This demonstrates that the fluid flow and mechanical deformation in porous media are closely interconnected each other.

Upon breakthrough or percolation, the invading fluid no longer needs to overcome the capillary pressure and invade new pores. Instead, a major portion of invading fluid flows out through the percolated pores, and it shows only a minor increase in fluid saturation. The inlet pressure shows no increase but a decrease, particularly a significant reduction in H-M coupled PNM, and it converges to a certain value after percolation (Fig. 5a). The reduced injection pressure upon percolation causes redistribution of pore pressure in the medium and hence slightly recover deformation though its extent is small (Fig. 5d). Figure 5e compares the different positions of grains at and after a while the percolation, and depicts the deformation recovery after percolation (or at capillary equilibrium).

Next, Fig. 6 shows the effect of the particle stiffness, in which the effective elastic modulus of solid particles varied from $E^* = 250 \text{ kPa}$ to 500 kPa , 5 MPa , and 50 MPa . An increase in the effective elastic modulus causes an increase in the spring stiffness K (Eq. 4).

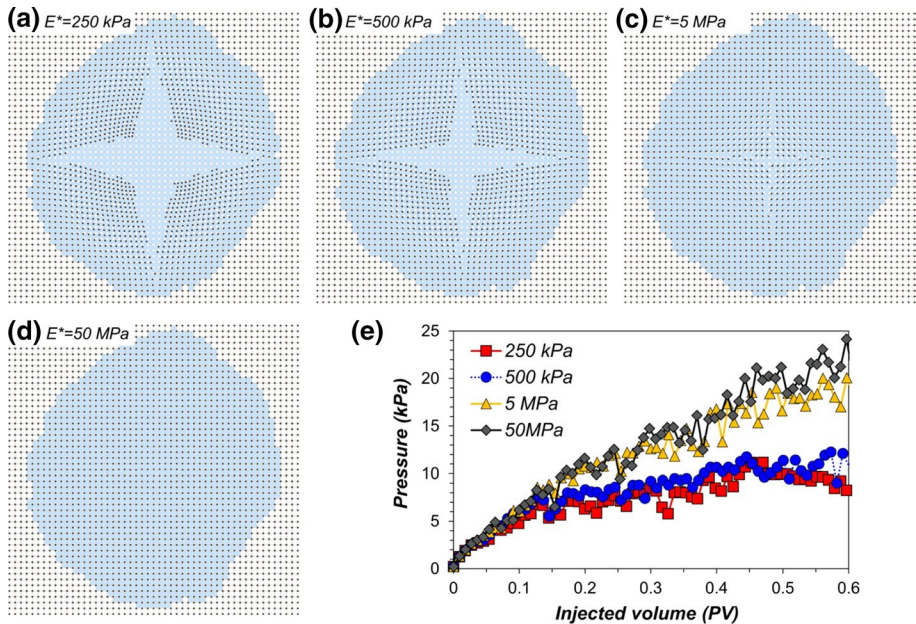


Fig. 6 Effect of the stiffness of solid particles on fluid propagation and solid deformation when the effective elastic modulus (E^*) is **a** 250 kPa, **b** 500 kPa, **c** 5 MPa, and **d** 50 MPa. **e** Evolutions of the injection pressure for various effective elastic modulus (E^*) of particles with respect to the injected pore volume

Therefore, the increased spring stiffness allows the less mechanical deformation with the smaller pore opening (see Fig. 6). The results again confirm that the mechanical deformations associated with pore opening cause reductions in the injection pressure, though the variations in the particle stiffness barely alter the fluid flow patterns. This implies that the softer porous media require the less injection pressure. Therefore, these observations suggest that the H-M coupling should be incorporated for analysis of fluid flows in soft deformable porous media.

4.2 Effect of Fluid Viscosity

Figure 7 shows the H-M PNM simulation results with different viscosity values μ of the invading fluid, from 0.01 (e.g., air) to 0.1 mPa·s (supercritical CO_2), 1 mPa·s (water), and 28 mPa·s (mineral oil). Herein, the flow rate Q of $10^{-6} \text{ m}^3/\text{s}$ and the interfacial tension of 45 m·Pa are used (Table 1). In addition, we also simulate the inviscid fluid flow for comparison, where the viscous pressure drops within the invading fluid are ignored (Fig. 7a).

The inviscid fluid flow simulation shows one extreme fingering pattern, in which the inviscid fluid flows through a preferential flow path (Fig. 7a). The injection pressure is very low, and thus, no deformation was observed in the porous medium. Accordingly, the pore saturation by the inviscid fluid in the pore-network is very low at percolation (i.e., low saturation). The number of fingers and fluid saturation slightly increase with the fluid viscosity; however, the fluid propagation patterns are similar to that of inviscid fluid with low saturation and insignificant deformation when the fluid viscosity values are low (e.g., $\mu = 0.01 \text{ mPa}\cdot\text{s}$ and $0.1 \text{ mPa}\cdot\text{s}$; Fig. 7b, c). The injection of fluids with the viscosity μ_{in}

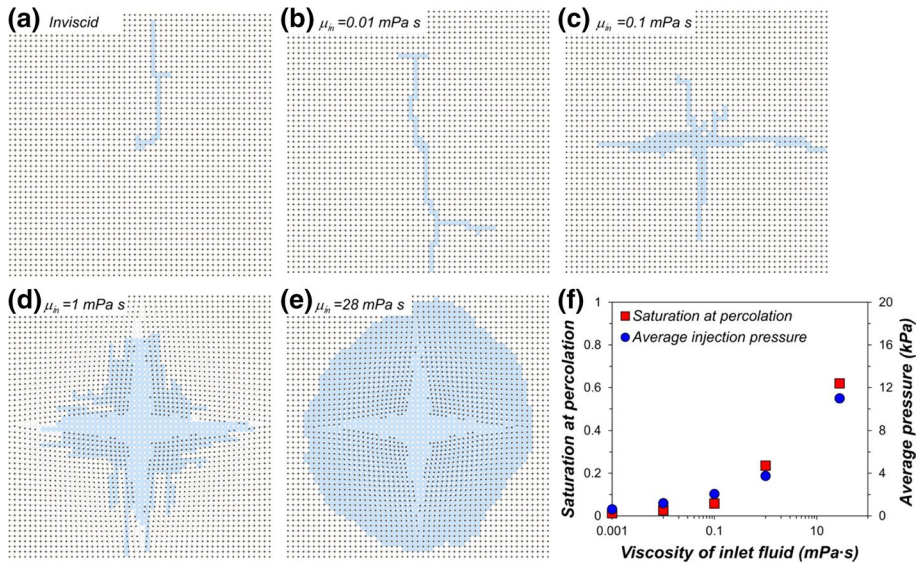


Fig. 7 Effect of the viscosity of invading fluids on the fluid propagation and solid deformation when the viscosity (μ_{in}) is **a** inviscid, **b** 0.01 mPa·s, **c** 0.1 mPa·s, **d** 1 mPa·s, and **e** 28 mPa·s. **f** The saturation of invading fluids at percolation and the average injection pressure with increasing viscosity. The values for inviscid fluid injection are plotted at $\mu_{in} = 0.001$ mPa·s

greater than 1 mPa·s causes radial fluid propagations accompanied by the improved saturations (Fig. 7d, e). At the same time, the injection pressure substantially rises to achieve the given flow rate, and the solid medium deformation becomes more prominent with the fracture-like cavity developed around the injection port (Fig. 7e). Herein, we observe a transition from the viscous fingering to the stable displacement, in which an increase in the invading fluid viscosity or mobility number Mo increases the fluid saturation (Fig. 7f), whereas, the increased viscosity also causes the injection pressure elevation and hence the deformation. These observations clearly demonstrate that the viscous pressure loss has a significant effect on the fluid propagation and concurrent solid medium deformation.

4.3 Effect of Flow Rate

We carry out another set of simulations while varying the flow rates Q from 10^{-10} , 10^{-8} , to 10^{-6} m³/s. The flow rate appears to have a minimal impact on the overall fluid propagation pattern, at least within the range of flow rates investigated in the simulations (Fig. 8a–c). Despite the low capillary number $Ca \ll 1$, the invading fluid flows radially, similar to the propagation pattern of the stable displacement regime, due to the high viscosity of the invading fluid (i.e., $\mu = 28$ mPa·s). Meanwhile, the higher flow rate causes the higher injection pressure. With that, larger deformation of solid develops as the flow rate increases from 10^{-10} to 10^{-6} m³/s, which can be intuitively expected because of the higher fluid pressure imposed at the inlet.

Severe fluctuations in the pressure responses take place when the flow rate Q is less than 10^{-8} m³/s (Fig. 8d). These pressure fluctuations are attributable to the phenomenon called Haines jump. When the flow rate is low (e.g., $Q < 10^{-8}$ m³/s), the rate of pressure

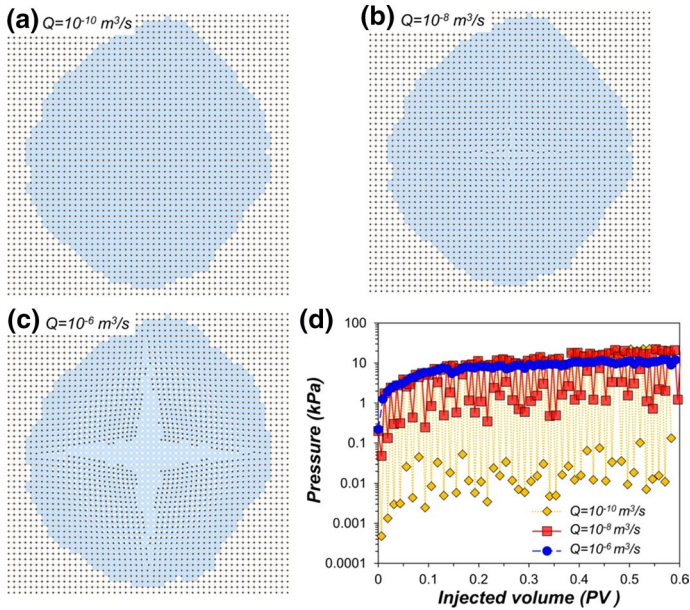


Fig. 8 Effect of injection flow rate on the fluid propagation and solid deformation. The flow rate is **a** $10^{-10} \text{ m}^3/\text{s}$, **b** $10^{-8} \text{ m}^3/\text{s}$, and **c** $10^{-6} \text{ m}^3/\text{s}$. **d** Variations in the injection pressure with respect to the injected pore volume for various injection flow rates

accumulation is slow. Therefore, the fluid pressure exhibits a gradual increase to overcome the capillary pressure. When the fluid pressure overcomes the capillary pressure and the fluid advances to the neighboring pore, the fluid pressure drops instantaneously, which is often referred to as the burst invasion. By contrast, the pressure rises quickly to achieve the imposed flow rate when the flow rate is high (e.g., $Q = 10^{-6} \text{ m}^3/\text{s}$). Therefore, the elevated pressure for the given flow rate suffices to overcome the capillary pressure at most of the throats, which minimizes the occurrence of Haines jump (compare the pressure fluctuations in Fig. 8d). It can be seen that the maximum (or peak) injection pressure values during the early times are very similar to each other regardless of the flow rate. It is because the capillary pressures of the pores with small throats determine the injection pressure and the viscous pressure drop is secondary. On the other hand, the high flow rate causes deformation with concurrent pore throat widening, and in turn, this deformation-induced pore throat widening decreases the capillary pressure. As a result, in the course of time, the peak pressure values under a high flow rate become less than those with low flow rates (Fig. 8d). Meanwhile, from a perspective of average pressure, the average injection pressure increases as the flow rate or velocity increases.

4.4 Effect of Structural Disorder

Lastly, we examine the effect of the structural disorder in the pore-network by applying different disorder coefficient λ from 0 (homogeneous), 0.1, 0.3, 0.5, 0.7, to 0.9. The throat radii of the pore-network are randomly generated in the range of $(1 - \lambda)a/2$ to $(1 + \lambda)a/2$ for

each case with a given λ . The total of 20 different randomly generated pore-networks are simulated to obtain statistically meaningful results for a given λ .

As shown in Fig. 9, the irregularity in the fluid propagation patterns becomes more distinct as λ increases. In the less disordered pore-networks (e.g., $\lambda=0-0.3$), the invading fluid propagates uniformly in a radial direction. In the more heterogeneous pore-networks with the greater disorder coefficient (e.g., $\lambda=0.5-0.9$), however, some pores in the vicinity of the inlet remain unfilled even after the fluid percolation. Note that the minimum throat radius becomes smaller as the disorder coefficient increases, such that some pores retain very small throat radii. High capillary pressure exerted at such small throats could prevent the fluid invasion into those pores. Consequently, the saturation of invading fluid at percolation decreases as λ increases (Fig. 10a).

A higher coefficient of structural disorder implies wider distributions of the pore throat size and their capillary pressures. Attributable to the more frequent occurrence of pores with small throats, the inlet pressure in average increases with an increase in λ though its variation also becomes greater (Fig. 10a). Figure 10b also shows that greater disorder in pore throat size can increase the injection pressure and cause more fluctuation with time. This temporal fluctuation and spatial variation in pore fluid pressure attribute to the extent of the poromechanical deformation. Greater heterogeneity (higher λ) leads to more severe temporal and spatial variations in pore pressures during fluid invasion. This eventually causes a more significant deformation (Fig. 9).

Although we only varied the throat radius in pore-networks with the disorder coefficient λ , the structural disorder or heterogeneity prevails in various geometric parameters of porous media, including but not limited to grain shape and size, pore shape and size, specific surface area, wettability, and local porosity. For an instance, pore throats in geologic porous materials are observed to have irregular shapes, and the corresponding capillary

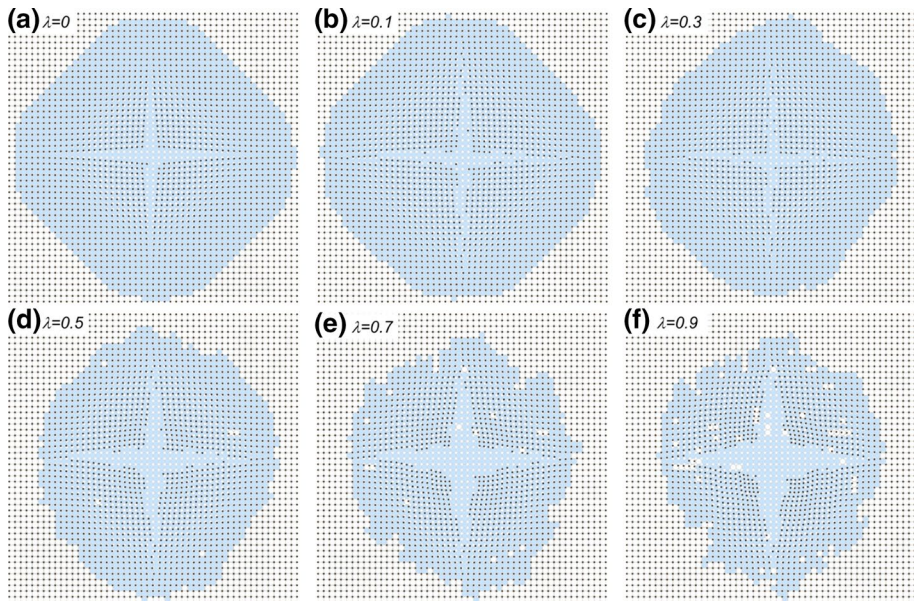


Fig. 9 Effect of the degree of structural disorder on fluid propagation and solid deformation when the disorder coefficient (λ) is **a** 0 (homogeneous), **b** 0.1, **c** 0.3, **d** 0.5, **e** 0.7, and **f** 0.9

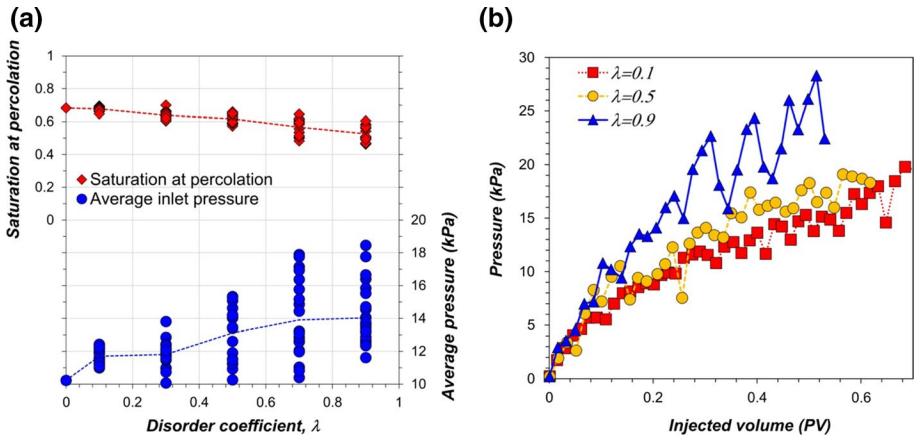


Fig. 10 Effect of the degree of structural disorder on **a** the saturation of invading fluids at percolation and the averaged injection pressure and **b** the evolutions of the injection pressure with injected fluid volume

pressure varies with its irregular throat shape (Suh et al. 2017). Each parameter may show a different and unique type of statistical distributions (e.g., Cui et al. 2019; Wang et al. 2019). Further research warrants to identify the effect of statistical distributions of pore-scale disorder on fluid-driven mechanical deformation.

4.5 Analyses on Dimensionless Parameters (Ca and Mo) and Particle-Level Forces

The two-phase fluid flows are greatly affected by the capillary number Ca and the mobility ratio Mo (Lenormand et al. 1988; Badillo et al. 2011; Zhang et al. 2011; Zheng et al. 2017; Chang et al. 2019). For the simulated cases, the capillary number Ca and the mobility number Mo are computed and plotted with the patterns of fluid invasion and mechanical deformation, as shown in Fig. 11. To be consistent, the cases with the disorder coefficient $\lambda=0.3$ are used for the dimensionless analysis. Besides nine aforementioned cases (Cases A-to-I), 11 additional H-M coupled PNM simulations with different input parameters are carried out (Cases J-to-T), and the results are included in Fig. 11. Table 2 complies the relevant dimensionless parameters for all the cases shown in Fig. 11. When computing the capillary number $Ca = \mu V / \sigma$, the average velocity is used for the velocity of invading fluid V owing to the radial flow condition adopted in this study.

The Ca value ranges approximately 10^{-8} – 10^{-1} , and the Mo value is in the range of 0.01–28. The capillary fingering is typically expected when $Ca < 10^{-5}$ – 10^{-6} (Lenormand et al. 1988; Badillo et al. 2011; Zhang et al. 2011; Zheng et al. 2017; Chang et al. 2019). Accordingly, Case M with $Ca = 2 \times 10^{-6}$ exhibits a capillary fingering effect. Cases J and N with $Ca < 10^{-7}$ and $Mo = 10^{-2}$ show the combined capillary and viscous fingering patterns of invading fluid. However, some cases, such as Cases P, O, H, and Q, hardly show fingering-like patterns even with low Ca value less than 10^{-4} , possibly because of the high mobility number Mo greater than 10.

The viscous fingering is expected when $Mo < 0.1$ and the stable displacement occurs when $Mo > 10$ (Lenormand et al. 1988; Badillo et al. 2011; Zhang et al. 2011; Zheng et al. 2017; Chang et al. 2019). In particular, our H-M PNM simulation results effectively capture the transition from the viscous fingering (e.g., Cases E and F) to the stable

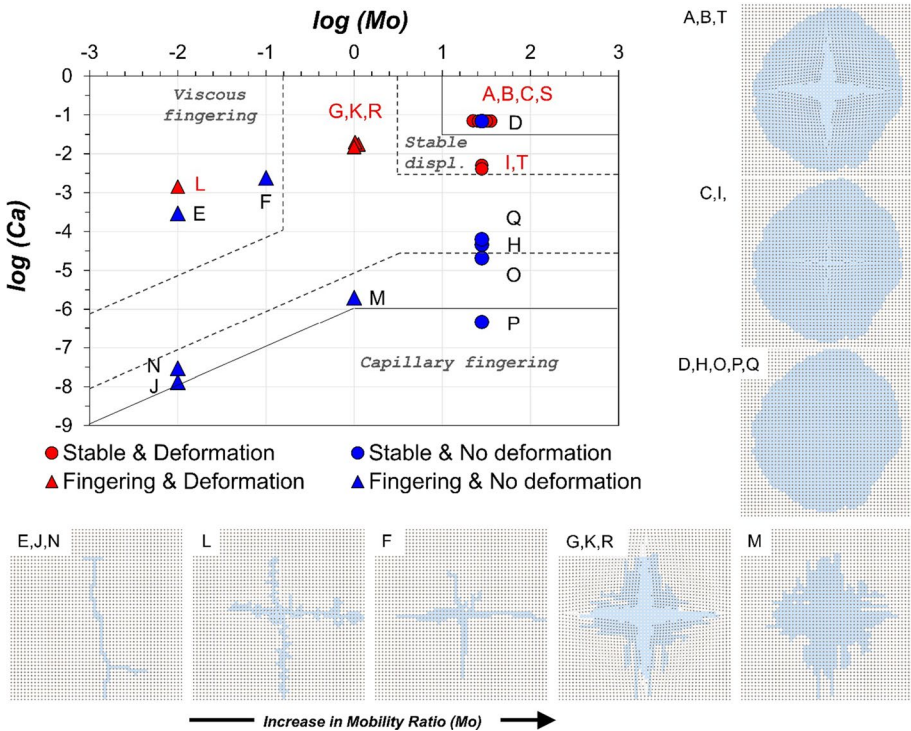


Fig. 11 Immiscible viscous fluid invasion and concurrent deformation in a $\log Ca$ - $\log Mo$ diagram. The boundaries for flow regimes are suggested by Lenormard et al. (1988, solid line) and Zhang et al. (2011, dash line)

displacement (e.g., Cases A and D) with the increased viscosity of the invading fluid. It can be seen that the fluid saturation increases with increasing viscosity (Figs. 7f, 11).

We further analyze the simulated fluid flow-driven deformation in relation to particle-level forces (e.g., Shin and Santamarina 2011; Han et al. 2019). The important particle-level forces include the seepage force F_s , the capillary force F_c , and the skeletal force F_{sk} . The seepage force F_s can be approximated by adopting Stokes' drag force produced by flow velocity V and fluid viscosity μ , i.e., $F_s = 6\pi\mu rV$, where r is the grain radius ($r = a$ in this study). The capillary force is caused by the interfacial tension σ between the immiscible fluids, $F_c = \pi d\sigma$, where d is the throat diameter ($d = a$ in this study). And, the skeletal force F_{sk} is defined as the force required to pull apart the compressed two grains with an initial spring contract h_o , following the Hertzian contact model, i.e., $F_{sk} = (4/3) \cdot E^* \cdot (r/2)^{1/2} \cdot h_o^{3/2}$. The relative ratios between these forces, F_s/F_{sk} and F_c/F_{sk} , can be adopted as indicators to occurrence of deformation for a given flow condition (Shin and Santamarina, 2011). Figure 12 plots the computed ratios with the deformation patterns for the simulated cases (Table 2). When the seepage force and capillary force are much smaller than the skeletal force, a fluid invades with no deformation (i.e., fluid invasion with no deformation). By contrast, when the capillary force is larger than the skeletal force, the elevated capillary force can promote opening of pores as fluid–fluid menisci wedge in between grains (i.e., capillary-driven deformation). When

Table 2 Summary of the dimensionless parameters for the simulated cases

Case	E^* (kPa)	μ_{in} (mPa·s)	q (m ³ /s)	IFT (mN/m)	Ca	Mo	F_s/F_{sk}	F_c/F_{sk}	Result figure
A	500	28	10^{-6}	45	7.06×10^{-2}	28	4.02×10^{-3}	9.48×10^{-3}	Figure 5c
B	250	28	10^{-6}	45	6.84×10^{-2}	28	7.78×10^{-3}	1.90×10^{-2}	Figure 6a
C	5000	28	10^{-6}	45	6.90×10^{-2}	28	3.92×10^{-4}	9.48×10^{-4}	Figure 6c
D	50,000	28	10^{-6}	45	6.90×10^{-2}	28	3.93×10^{-5}	9.48×10^{-5}	Figure 6d
E	500	0.01	10^{-6}	45	2.94×10^{-4}	0.01	1.67×10^{-5}	9.48×10^{-3}	Figure 7b
F	500	0.1	10^{-6}	45	2.39×10^{-3}	0.1	1.36×10^{-4}	9.48×10^{-3}	Figure 7c
G	500	1	10^{-6}	45	1.74×10^{-2}	1	9.89×10^{-4}	9.48×10^{-3}	Figure 7d
H	500	28	10^{-10}	45	4.61×10^{-5}	28	2.62×10^{-6}	9.48×10^{-3}	Figure 8a
I	500	28	10^{-8}	45	4.57×10^{-3}	28	2.60×10^{-4}	9.48×10^{-3}	Figure 8b
J	500	0.01	10^{-10}	100	1.32×10^{-8}	0.01	1.67×10^{-9}	2.11×10^{-2}	Additional cases
K	10,000	1	10^{-6}	45	2.00×10^{-2}	1	5.68×10^{-5}	4.74×10^{-4}	
L	500	0.01	10^{-4}	45	1.42×10^{-3}	0.01	8.07×10^{-5}	9.48×10^{-3}	
M	500	1	10^{-10}	45	1.99×10^{-6}	1	1.13×10^{-7}	9.48×10^{-3}	
N	500	0.01	10^{-10}	45	2.94×10^{-8}	0.01	1.67×10^{-9}	9.48×10^{-3}	
O	500	28	10^{-10}	100	2.08×10^{-5}	28	2.63×10^{-6}	2.11×10^{-2}	
P	500	28	10^{-12}	45	4.61×10^{-7}	28	2.62×10^{-8}	9.48×10^{-3}	
Q	5000	28	10^{-10}	45	4.61×10^{-5}	28	2.62×10^{-7}	9.48×10^{-4}	
R	50	1	10^{-6}	45	1.50×10^{-2}	1	8.52×10^{-3}	9.48×10^{-2}	
S	10,000	28	10^{-6}	45	6.90×10^{-2}	28	1.96×10^{-4}	4.74×10^{-4}	
T	200	28	10^{-8}	45	4.06×10^{-3}	28	5.78×10^{-4}	2.37×10^{-2}	

The capillary number Ca is defined as $V \cdot \mu_{in} / \sigma$, and the viscosity ratio M is defined as μ_{in} / μ_{net} . F_s is the seepage force, F_c is the capillary force, and F_{sk} is the skeletal force, represented by the effective stiffness E^* . F_{sk} is defined as $(4/3) \cdot E^* \cdot (a/2)^{1/2} \cdot h_0^{3/2}$ following the Hertzian contact model, F_c is defined as $2\pi r\sigma$, and F_s is defined as $\delta\pi\mu aV$ following the Stokes' drag force

a sufficient drag force by seepage is developed to overcome the skeletal force, deformation can also occur (i.e., drag-driven deformation).

Our results clearly reveal two different regimes: fluid invasion with no deformation versus drag-driven deformation (Fig. 12). When F_s/F_{sk} is less than $\sim 10^{-5}$, no deformation is observed. When F_s/F_{sk} is greater than 10^{-4} , the viscous drag force appears to be sufficient to cause deformation. It is consistently found that the extent of deformation becomes more prominent with increasing F_s/F_{sk} . By contrast, the capillary force hardly gains relevance in the simulated range when $F_c/F_{sk} < 0.1$. We find that our H-M coupled PNM well captures the interactions between the particle-level forces postulated above, particularly the seepage force (viscous drag) versus the skeletal force.

5 Conclusion

We develop a two-way coupled H-M PNM that accounts for the viscous pressure loss and concurrent poromechanical deformation during fluid flows. In both single- and two-phase flow conditions, the results from H-M PNM simulations and experiments show good agreement, which supports that the developed H-M PNM can properly capture the behavior of

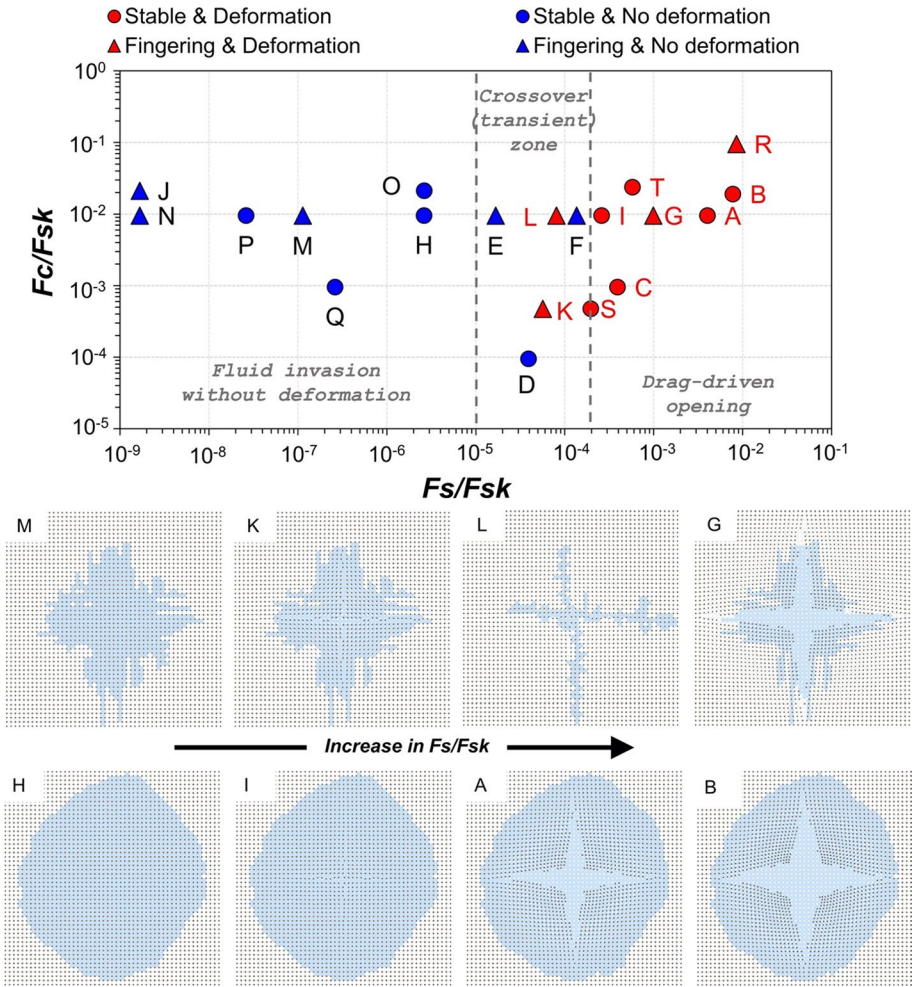


Fig. 12 Mechanical deformation regimes depending on the balance between the particle-level forces. The capillary force is defined as $F_c = 2\pi r\sigma$, the seepage force (or Stoke’s drag force) is $F_s = 6\pi\mu aV$, and the skeletal force is $F_{sk} = (4/3) \cdot E^* \cdot (a/2)^{1/2} \cdot h^{3/2}$

fluids and solids that constitute the deformable porous medium. We conduct parametric studies to elucidate the effects of mechanical coupling, stiffness of solid particles, fluid viscosity, injection rate, and structural disorder on the fluid flow and concurrent solid medium deformation. Mechanical deformation reduces the injection pressure via the pore opening, whereas mechanical coupling barely affects the flow patterns. The required injection pressure becomes less with a softer porous medium during viscous fluid injection. The viscosity of invading fluid, on the other hand, has a substantial influence on not only pressure but also the flow patterns. The injection rate has little impact on the flow pattern in the tested regime, but larger deformation occurs as the injection rate increases. Lastly, the pattern of fluid propagation becomes more irregular, and the saturation of invading fluid decreases as the degree of structural disorder intensifies. The average injection pressure increases with the higher structural disorder, and the pressure fluctuation becomes more severe,

which results in the larger deformation of solids. The results imply that the poromechanical deformation is affected not only by the magnitude of injection pressure but also by ensuing pressure fluctuation. The analysis with dimensionless numbers confirms that our results are placed over a wide range of the mobility ratio, including a transition from the viscous fingering to the stable displacement with increasing viscosity. The observations from the PNM simulations suggested that the H-M coupling provided deeper insights into patterns of fluid flows and deformations upon the reflection of the stiffness, heterogeneity of porous media, and fluid injection rate. The particle-level force analysis clearly reveals two distinct regimes: a regime of fluid invasion with no deformation and a regime of drag-driven deformation. Our H-M coupled PNM well captures the deformation associated with interactions between the seepage force (viscous drag) and the skeletal force. The H-M PNM is applicable to various fields where the poromechanical deformation is expected during the fluid injection.

Acknowledgements We would like to thank three anonymous reviewers for providing valuable comments and suggests, which was very helpful to improve this manuscript. This research was supported by the Basic Research Laboratory Program through the National Research Foundation of Korea (NRF) funded by the MSIT (NRF-2018R1A4A1025765) and by Korea Ministry of Land, Infrastructure and Transport (MOLIT) as “Innovative Talent Education Program for Smart City.”

References

- Aker, E., JØrgen MÅlØy, K., Hansen, A., Batrouni, G.G.: A two-dimensional network simulator for two-phase flow in porous media. *Transp. Porous Media* **32**(2), 163–186 (1998). <https://doi.org/10.1023/a:1006510106194>
- Atrazhev, V.V., Astakhova, T.Y., Dmitriev, D.V., Erikhman, N.S., Sultanov, V.I., Patterson, T., Burlat-sky, S.F.: The model of stress distribution in polymer electrolyte membrane. *J. Electrochem. Soc.* **160**(10), F1129–F1137 (2013)
- Badillo, G.M., Segura, L.A., Laurindo, J.B.: Theoretical and experimental aspects of vacuum impregnation of porous media using transparent etched networks. *Int. J. Multiph. Flow* **37**(9), 1219–1226 (2011). <https://doi.org/10.1016/j.ijmultiphaseflow.2011.06.002>
- Blunt, M.J.: Flow in porous media—pore-network models and multiphase flow. *Curr. Opin. Colloid Interface Sci.* **6**(3), 197–207 (2001)
- Budday, S., Nay, R., de Rooij, R., Steinmann, P., Wyrobek, T., Ovaert, T.C., Kuhl, E.: Mechanical properties of gray and white matter brain tissue by indentation. *J. Mech. Behav. Biomed. Mater.* **46**, 318–330 (2015). <https://doi.org/10.1016/j.jmbbm.2015.02.024>
- Chang, C., Kneafsey, T.J., Zhou, Q., Oostrom, M., Ju, Y.: Scaling the impacts of pore-scale characteristics on unstable supercritical CO₂-water drainage using a complete capillary number. *Int. J. Greenhouse Gas Control* **86**, 11–21 (2019). <https://doi.org/10.1016/j.ijggc.2019.04.010>
- Cui, G., Liu, M., Dai, W., Gan, Y.: Pore-scale modelling of gravity-driven drainage in disordered porous media. *Int. J. Multiph. Flow* **114**, 19–27 (2019). <https://doi.org/10.1016/j.ijmultiphaseflow.2019.02.001>
- Fatt, I.: The network model of porous media. (1956)
- Franceschini, G., Bigoni, D., Regitnig, P., Holzapfel, G.A.: Brain tissue deforms similarly to filled elastomers and follows consolidation theory. *J. Mech. Phys. Solids* **54**(12), 2592–2620 (2006)
- Haines, W.B.: Studies in the physical properties of soil. V. The hysteresis effect in capillary properties, and the modes of moisture distribution associated therewith. *J. Agric. Sci.* **20**(1), 97–116 (1930). <https://doi.org/10.1017/s002185960008864x>
- Han, G., Kwon, T.-H., Lee, J.Y., Jung, J.: Fines migration and pore clogging induced by single- and two-phase fluid flows in porous media: from the perspectives of particle detachment and particle-level forces. *Geomech. Energy Environ.* (2019). <https://doi.org/10.1016/j.gete.2019.100131>
- Holtzman, R., Juanes, R.: Crossover from fingering to fracturing in deformable disordered media. *Phys. Rev. E* **82**(4), 046305 (2010)

- Holtzman, R., Juanes, R.: Thermodynamic and hydrodynamic constraints on overpressure caused by hydrate dissociation: a pore-scale model. *Res. Lett., Geophys* (2011). <https://doi.org/10.1029/2011g1047937>
- Hosseini Zadeh, A., Jeon, M.K., Kwon, T.H., Kim, S.: Study of poroelastic deformation in soft elastic granular materials during repetitive fluid injection. In: Paper presented at the 53rd U.S. Rock Mechanics/Geomechanics Symposium, New York City, New York (2019)
- Johnson, K.L.: *Contact Mechanics*. Cambridge University Press, Cambridge (1987)
- Kharaghani, A., Metzger, T., Tsotsas, E.: A proposal for discrete modeling of mechanical effects during drying, combining pore networks with DEM. *AIChE J.* **57**(4), 872–885 (2011). <https://doi.org/10.1002/aic.12318>
- Lee, D., Ryu, S.: A Validation study of the repeatability and accuracy of atomic force microscopy indentation using polyacrylamide gels and colloidal probes. *J. Biomech. Eng.* doi **10**(1115/1), 4035536 (2017)
- Lenormand, R., Touboul, E., Zarcone, C.: Numerical models and experiments on immiscible displacements in porous media. *J. Fluid Mech.* **189**, 165–187 (1988)
- Lindquist, W.B., Venkatarangan, A.: Investigating 3D geometry of porous media from high resolution images. *Phys. Chem. Earth Part A.* **24**(7), 593–599 (1999). [https://doi.org/10.1016/S1464-1895\(99\)00085-X](https://doi.org/10.1016/S1464-1895(99)00085-X)
- MacMinn, C.W., Dufresne, E.R., Wettlaufer, J.S.: Fluid-driven deformation of a soft granular material. *Phys. Rev. X* **5**(1), 011020 (2015)
- Mahabadi, N., Jang, J.: The impact of fluid flow on force chains in granular media. *Appl. Phys. Lett.* **110**(4), 041907 (2017). <https://doi.org/10.1063/1.4975065>
- Maier, R., Laidlaw, W.G.: Fluid percolation in bond-site size-correlated three-dimensional networks. *Transp. Porous Media* **5**(4), 421–428 (1990). <https://doi.org/10.1007/BF01141994>
- Massonnet, D., Holzer, T., Vadon, H.: Land subsidence caused by the East Mesa Geothermal Field, California, observed using SAR interferometry. *Geophys. Res. Lett.* **24**(8), 901–904 (1997). <https://doi.org/10.1029/97g100817>
- Pan, P., Wu, Z., Feng, X., Yan, F.: Geomechanical modeling of CO₂ geological storage: a review. *J. Rock Mech. Geotech. Eng.* **8**(6), 936–947 (2016). <https://doi.org/10.1016/j.jrmge.2016.10.002>
- Pandey, S.N., Chaudhuri, A., Kelkar, S.: A coupled thermo-hydro-mechanical modeling of fracture aperture alteration and reservoir deformation during heat extraction from a geothermal reservoir. *Geothermics* **65**, 17–31 (2017). <https://doi.org/10.1016/j.geothermics.2016.08.006>
- Reeves, P.C., Celia, M.A.: A functional relationship between capillary pressure, saturation, and interfacial area as revealed by a pore-scale network model. *Water Resour. Res.* **32**(8), 2345–2358 (1996)
- Shin, H., Santamarina, J.C.: Desiccation cracks in saturated fine-grained soils: particle-level phenomena and effective-stress analysis. *Géotechnique* **61**(11), 961–972 (2011). <https://doi.org/10.1680/geot.8.P.012>
- Silin, D., Tomutsa, L., Benson, S.M., Patzek, T.W.: Microtomography and pore-scale modeling of two-phase fluid distribution. *Transp. Porous Media* **86**(2), 495–515 (2011). <https://doi.org/10.1007/s11242-010-9636-2>
- Silin, D.B., Jin, G., Patzek, T.W.: Robust determination of the pore space morphology in sedimentary rocks. In: Paper presented at the SPE Annual Technical Conference and Exhibition, Denver, Colorado (2003)
- Simms, P., Yanful, E.: A pore-network model for hydromechanical coupling in unsaturated compacted clayey soils. *Can. Geotech. J.* **42**(2), 499–514 (2005)
- Stan, C.A., Tang, S.K.Y., Whitesides, G.M.: Independent control of drop size and velocity in microfluidic flow-focusing generators using variable temperature and flow rate. *Anal. Chem.* **81**(6), 2399–2402 (2009). <https://doi.org/10.1021/ac8026542>
- Streit, J.E., Hillis, R.R.: Estimating fault stability and sustainable fluid pressures for underground storage of CO₂ in porous rock. *Energy* **29**(9), 1445–1456 (2004). <https://doi.org/10.1016/j.energy.2004.03.078>
- Støverud, K.H., Darcis, M., Helmig, R., Hassanizadeh, S.M.: Modeling concentration distribution and deformation during convection-enhanced drug delivery into brain tissue. *Transp. Porous Media* **92**(1), 119–143 (2012)
- Suh, H.S., Kang, D.H., Jang, J., Kim, K.Y., Yun, T.S.: Capillary pressure at irregularly shaped pore throats: implications for water retention characteristics. *Adv. Water Resour.* **110**, 51–58 (2017). <https://doi.org/10.1016/j.advwatres.2017.09.025>
- Vogel, H.-J., Tölke, J., Schulz, V.P., Krafczyk, M., Roth, K.: Comparison of a Lattice-Boltzmann model, a full-morphology model, and a pore network model for determining capillary pressure-saturation relationships. *Vadose Zone J.* **4**(2), 380–388 (2005). <https://doi.org/10.2136/vzj2004.0114>

- Wang, Z., Chauhan, K., Pereira, J.-M., Gan, Y.: Disorder characterization of porous media and its effect on fluid displacement. *Phys. Rev. Fluids* **4**(3), 034305 (2019). <https://doi.org/10.1103/PhysRevFluids.4.034305>
- Zhang, C., Oostrom, M., Wietsma, T.W., Grate, J.W., Warner, M.G.: Influence of viscous and capillary forces on immiscible fluid displacement: pore-scale experimental study in a water-wet micromodel demonstrating viscous and capillary fingering. *Energy Fuels* **25**(8), 3493–3505 (2011)
- Zheng, X., Mahabadi, N., Yun, T.S., Jang, J.: Effect of capillary and viscous force on CO₂ saturation and invasion pattern in the microfluidic chip. *J. Geophys. Res. Solid Earth* **122**(3), 1634–1647 (2017). <https://doi.org/10.1002/2016jb013908>

Publisher's Note Springer Nature remains neutral with regard to jurisdictional claims in published maps and institutional affiliations.

Affiliations

Min-Kyung Jeon¹ · Seunghee Kim²  · Amin Hosseini Zadeh² · Tae-Hyuk Kwon¹ 

Min-Kyung Jeon
gmk909@kaist.ac.kr

Amin Hosseini Zadeh
amin.hosseini-zadeh@huskers.unl.edu

¹ Department of Civil and Environmental Engineering, Korea Advanced Institute of Science and Technology (KAIST), Daejeon, Korea

² Department of Civil and Environmental Engineering, University of Nebraska-Lincoln, Omaha, NE, USA